

Resonant Raman spectra of diindenoperylene thin films

R. Scholz,^{1,2,a)} L. Gisslén,² B.-E. Schuster,³ M. B. Casu,³ T. Chassé,³ U. Heinemeyer,⁴ and F. Schreiber⁴¹Walter Schottky Institut und Physik Department, Technische Universität München, 85748 Garching, Germany²Institut für Angewandte Photophysik, Technische Universität Dresden, 01062 Dresden, Germany³Institut für Physikalische und Theoretische Chemie, Universität Tübingen, Auf der Morgenstelle 18, 72076 Tübingen, Germany⁴Institut für Angewandte Physik, Universität Tübingen, Auf der Morgenstelle 10, 72076 Tübingen, Germany

(Received 6 July 2010; accepted 21 October 2010; published online 4 January 2011)

Resonant and preresonant Raman spectra obtained on diindenoperylene (DIP) thin films are interpreted with calculations of the deformation of a relaxed excited molecule with density functional theory (DFT). The comparison of excited state geometries based on time-dependent DFT or on a constrained DFT scheme with observed absorption spectra of dissolved DIP reveals that the deformation pattern deduced from constrained DFT is more reliable. Most observed Raman peaks can be assigned to calculated A_g -symmetric breathing modes of DIP or their combinations. As the position of one of the laser lines used falls into a highly structured absorption band, we have carefully analyzed the Raman excitation profile arising from the frequency dependence of the dielectric tensor. This procedure gives Raman cross sections in good agreement with the observed relative intensities, both in the fully resonant and in the preresonant case. © 2011 American Institute of Physics. [doi:10.1063/1.3514709]

I. INTRODUCTION

Due to various device applications ranging from light emitting diodes over photovoltaic cells to organic field effect transistors, organic semiconducting thin films have attracted significant attention. An important prerequisite for device applications are molecular films with reproducible morphology, depending however on various growth parameters like the reactivity of the substrates, growth temperature, and deposition rate. For crystalline organic materials, microscopic interpretations of charge transport and optical properties rely heavily on the previous knowledge of the arrangement of the molecules in the crystal unit cell, as determined, e.g., by x-ray diffraction.

Diindenoperylene (DIP), synthesized as early as in 1937,¹ has received renewed attention due to relatively high charge carrier mobilities,^{2,3} well defined ordering of thin films,⁴ the existence of two polymorphs,⁵ and interesting growth properties.^{6,7} From a comparison of thin films with these polymorphs, it turned out that the thin film phase corresponds to a substrate-stabilized high-temperature phase.⁵ In a recent investigation of the optical response of dissolved DIP and crystalline thin films, we have shown that the vibronic progression of the dissolved chromophore is modified in the solid, revealing the formation of Frenkel excitons and their interference with charge transfer (CT) states.^{8,9} Nevertheless, even in the crystalline phase, the largest parameters involved in the calculated shape of the optical response arise from the deformation of a DIP molecule in its relaxed excited geometry.

Preresonant and resonant Raman spectroscopy in the region of a strong dipole-allowed transition gives detailed information on the projection of the deformation of a molecule in its relaxed excited geometry onto internal vibrations. Therefore, Raman spectra are complementary to optical absorption and photoluminescence (PL), where elongations of internal vibrations in an excited molecule give rise to pronounced vibronic progressions together with a Stokes shift between the average excitation and de-excitation energies. After the Raman process, the molecule returns to an excited vibrational level in its electronic ground state, so that in principle, the Raman modes coincide with the vibronic sidebands observed in fluorescence. However, only under favorable conditions like single molecules embedded in droplets of superfluid helium or in Shpol'skii matrices, the vibronic features of the fluorescence or fluorescence excitation spectra can be observed with high resolution,¹⁰⁻¹² whereas the optical spectra of chromophores dissolved in typical solvents suffer from a large broadening arising from fluctuations of the surrounding solvent molecules. Hence, sidebands of individual vibrational modes cannot be resolved because they merge into broad Gaussian bands. For these reasons, Raman spectroscopy is the method of choice for an investigation of the coupling between optical excitations and internal vibrations of a molecule. Together with calculations based on density functional theory (DFT), a microscopic assignment of the observed features to specific internal vibrations can be obtained.

In Sec. II, we present the theoretical background of resonant and preresonant Raman spectra. Section III is devoted to the experimental results obtained on DIP films which are interpreted in Sec. IV with density functional calculations of the deformation of a DIP molecule in its relaxed excited geometry. Deviations between different resonance conditions are

^{a)}Authors to whom correspondence should be addressed. Electronic mail: reinhard.scolz@iapp.de.

analyzed in Sec. V. The main achievements of the present work are summarized in Sec. VI.

II. THEORETICAL BACKGROUND

A. Deformation of an excited molecule

The geometry of a molecule depends on its electronic configuration, so that the electronic ground state and the lowest excited state after a HOMO–LUMO transition correspond to slightly different shapes. From a projection of the respective deformation onto the vibrational eigenvectors, the reorganization energy λ on the ground or excited state potential surface can be decomposed into contributions of different vibrational modes according to

$$\lambda = \sum_k S_k \hbar \omega_k, \quad (1)$$

where ω_k is the vibrational frequency and S_k the Huang–Rhys factor of mode k . Density functional calculations addressing these quantities will be discussed in Sec. IV.

B. Raman cross sections

The present work concentrates on the dominating Raman cross sections arising from breathing modes, so that all except for the lowest modes have energies well above thermal energy at room temperature. Therefore, in the following, we shall present the equations underlying Raman spectroscopy under the assumption that all breathing modes are in the vibrational ground state, and known correction factors at finite temperature will be added in the final equations. At zero temperature, the differential cross section of the Stokes Raman process can be expressed as^{13–16}

$$\begin{aligned} \frac{d\sigma(\omega_L, \omega_s)}{d\Omega} &= \sum_f \frac{\omega_L \omega_s^3}{16\pi^2 \epsilon_0^2 \hbar^2 c^4} \\ &\times \left| \sum_m \left[\frac{\langle f | \mathbf{e}_s \cdot \hat{\boldsymbol{\mu}} | m \rangle \langle m | \mathbf{e}_L \cdot \hat{\boldsymbol{\mu}} | i \rangle}{\omega_m - \omega_i - \omega_L - i\gamma} \right. \right. \\ &\left. \left. + \frac{\langle f | \mathbf{e}_s \cdot \hat{\boldsymbol{\mu}} | m \rangle \langle m | \mathbf{e}_L \cdot \hat{\boldsymbol{\mu}} | i \rangle}{\omega_m - \omega_i + \omega_L + i\gamma} \right] \right|^2, \quad (2) \end{aligned}$$

where ω_L and ω_s are the incident and scattered frequencies, and \mathbf{e}_L and \mathbf{e}_s the corresponding polarization vectors. The initial state $|i\rangle$ is the lowest vibrational level in the electronic ground state, and the final state $|f\rangle$ may contain excited vibrational levels in the electronic ground state, where, in the following, we shall concentrate on excitations containing only a single vibrational quantum of an arbitrary internal breathing mode. The intermediate state $|m\rangle$ is a vibrational level of the excited state coupled by the dipole operator $\hat{\boldsymbol{\mu}}$ to the electronic ground state.

Equation (2) can be evaluated most easily if the excited state potential of a molecule consists of a sum over displaced harmonic oscillators for all symmetry-conserving internal modes. Under the additional assumption of vanishing Dushinsky rotations, a transition dipole independent of the nuclear geometry, and the same vibrational frequencies on

both potential energy surfaces involved, the matrix elements for excitation of a single vibration $\hbar\omega_k$ factorize into contributions of different internal modes,

$$\langle m | \hat{\boldsymbol{\mu}} | i \rangle = \boldsymbol{\mu}_{eg} \langle m_k^{(e)} | 0_k^{(g)} \rangle \prod_{j \neq k} \langle m_j^{(e)} | 0_j^{(g)} \rangle, \quad (3)$$

$$\langle f | \hat{\boldsymbol{\mu}} | m \rangle = \boldsymbol{\mu}_{ge} \langle 1_k^{(g)} | m_k^{(e)} \rangle \prod_{j \neq k} \langle 0_j^{(g)} | m_j^{(e)} \rangle, \quad (4)$$

with the abbreviation $\boldsymbol{\mu}_{eg} = \langle e | \hat{\boldsymbol{\mu}} | g \rangle$ for the transition dipole, and similarly for its adjoint. The superscript e stands for the excited state, and g for the ground state, and $|m_k^{(e)}\rangle$ denotes the vibrational level m of mode k in the excited potential. The Franck–Condon factors $\langle m_j^{(e)} | 0_j^{(g)} \rangle$ can be obtained from the Poisson progression over the transition probabilities involved in absorption,

$$P(|0_j^{(g)}\rangle \rightarrow |m_j^{(e)}\rangle) = |\langle m_j^{(e)} | 0_j^{(g)} \rangle|^2 = e^{-S_j} \frac{S_j^{m_j^{(e)}}}{m_j^{(e)}!}, \quad (5)$$

where the Huang–Rhys factor S_j of each mode can be deduced from its contribution $S_j \hbar \omega_j$ to the reorganization energy λ . In Eqs. (2)–(4), each mode $j \neq k$ returning to its lowest vibrational level after the scattering process gives a matrix element coinciding with the normalized transition probability observed in absorption according to Eq. (5). The product of the Franck–Condon factors of the vibrational mode k excited by the scattering process can be calculated as¹⁶

$$\begin{aligned} \langle 1_k^{(g)} | m_k^{(e)} \rangle \langle m_k^{(e)} | 0_k^{(g)} \rangle & \\ &= e^{-S_k} \sqrt{S_k} \frac{S_k^{m_k^{(e)}} - m_k^{(e)} S_k^{m_k^{(e)}-1}}{m_k^{(e)}!}. \quad (6) \end{aligned}$$

C. Preresonant Raman spectra

A compact evaluation of the sum over intermediate states in Eq. (2) can only be obtained in the preresonant case. Replacing all modes except for the mode k by a detuning δ with respect to the laser frequency ω_L ,

$$\delta = \omega_{00} + \sum_{j \neq k} m_j^{(e)} \omega_j - \omega_L \quad (7)$$

the resonance denominator can be expanded into a Taylor series,

$$\begin{aligned} \frac{1}{\omega_m - \omega_i - \omega_L - i\gamma} &= \frac{1}{\delta + m_k^{(e)} \omega_k - i\gamma} \\ &\approx \frac{1}{\delta} \left(1 - \frac{m_k^{(e)} \omega_k}{\delta} \right). \quad (8) \end{aligned}$$

Inserting this Taylor series expansion and the expression (6) into the sum in Eq. (2), the lowest order gives a vanishing contribution, but the first order results in

$$- \frac{1}{\delta^2} \sum_{m_k^{(e)}} m_k^{(e)} \omega_k \langle 1_k^{(g)} | m_k^{(e)} \rangle \langle m_k^{(e)} | 0_k^{(g)} \rangle = \frac{\sqrt{S_k} \omega_k}{\delta^2}. \quad (9)$$

Taking an average over the detunings, $\langle 1/\delta^2 \rangle$, the absolute square of the sum in Eq. (2) gives the following Raman cross section

$$\frac{d\sigma(\omega_L)}{d\Omega} = \frac{\omega_L \omega_s^3}{16\pi^2 \varepsilon_0^2 \hbar^2 c^4} (\mathbf{e}_s \cdot \hat{\boldsymbol{\mu}}_{ge})^2 \times (\mathbf{e}_L \cdot \hat{\boldsymbol{\mu}}_{eg})^2 S_k \omega_k^2 \left\langle \frac{1}{\delta^2} \right\rangle^2, \quad (10)$$

where in the average $\langle 1/\delta^2 \rangle$ each vibrational level in the excited state contributes according to the product of the transition probabilities defined in Eq. (5). The fact that the cross section is proportional to $\langle 1/\delta^2 \rangle^2$ gives a direct measure of the large resonance enhancement of the Raman signal when the detuning from full resonance is decreased. At finite temperature, the cross section for Stokes Raman scattering increases due to the thermal occupation of each mode,

$$\frac{d\sigma(\omega_L)}{d\Omega} \propto S_k \omega_k^2 [1 + n_{th}(\hbar\omega_k, k_B T)] \left\langle \frac{1}{\delta^2} \right\rangle^2. \quad (11)$$

D. Resonant Raman spectra

In the fully resonant case, the Taylor series expansion in Eq. (8) cannot be used, so that the resulting cross section will differ from the compact result in Eq. (11). The analytical derivation summarized in Sec. II B relies on the assumption of independent molecules,¹⁶ with an excited state potential consisting of displaced harmonic oscillators for internal breathing modes which can easily be parameterized. Albeit, in the crystalline phase, the optical response of a single molecule is modified by transfer of optical excitations between neighboring sites and by the interference between neutral excitations and inter-molecular CT states, so that the Hamiltonian for the excited electronic state does not factorize into independent internal modes. Instead, the transfer of neutral excitations between different sites and the coupling to CT states is formulated in terms of an *effective* internal vibration, with energy and *effective* Huang–Rhys factor corresponding to the vibronic progression observed for dissolved DIP molecules.^{8,9} Therefore, at the present stage, it is not possible to provide an excited state Hamiltonian allowing to determine the vibrational levels $|m\rangle$ required in Eq. (2).

In cases where a suitable Hamiltonian for the excited state is not known in sufficient detail, it was demonstrated that the so-called transform theory can be used to derive resonance profiles of Raman spectra from the polarizability.^{17,18} The basic ingredients can be motivated from the transformation of the resonant part of the cross section in Eq. (2) into the time domain, neglecting the off-resonant part altogether. This allows to express the cross section for Stokes Raman scattering in the form

$$\frac{d\sigma(\omega_L, \omega_s)}{d\Omega} \propto S_k [1 + n_{th}(\hbar\omega_k, k_B T)] |\Phi(\omega_L) - \Phi(\omega_s)|^2, \quad (12)$$

where Φ is the resonant part of the complex polarizability, n_{th} the thermal occupation of the vibrational mode k excited

by Raman scattering, and the scattered frequency ω_s is red-shifted by the frequency ω_k of this mode, $\omega_s = \omega_L - \omega_k$.¹⁷ The polarizability Φ can be obtained from the resonant part of the complex dielectric tensor, multiplied from both sides with the polarization vectors \mathbf{e}_L or \mathbf{e}_s of incident and scattered light, respectively:

$$\Phi(\omega_L) = \mathbf{e}_s \cdot \overset{\leftrightarrow}{\epsilon}(\omega_L) \cdot \mathbf{e}_L, \quad (13)$$

$$\Phi(\omega_s) = \mathbf{e}_s \cdot \overset{\leftrightarrow}{\epsilon}(\omega_s) \cdot \mathbf{e}_L. \quad (14)$$

Transform theory of Raman cross sections was applied successfully to molecules with a rather structured absorption lineshape, so that the difference between the polarizabilities at the laser frequency ω_L and at the frequency of the scattered light ω_s results in strongly modulated Raman excitation profiles.^{16,18–20} In the opposite limit of broad unmodulated absorption bands, transform theory according to Eq. (12) correctly predicts structureless Raman excitation profiles resembling the absorption lineshape.^{21,22} In these cases, the difference between the polarizabilities in Eq. (12) can be replaced to leading order by the derivative at the midpoint between ω_L and ω_s ,

$$\Phi(\omega_L) - \Phi(\omega_s) \approx \omega_k \Phi' \left(\frac{\omega_L + \omega_s}{2} \right), \quad (15)$$

where the difference between incident and scattered frequencies has been expressed by the frequency of the excited vibration, $\omega_k = \omega_L - \omega_s$. Inserting this approximation into the Raman cross section, one finds

$$\frac{d\sigma(\omega)}{d\Omega} \propto S_k (\hbar\omega_k)^2 [1 + n_{th}(\hbar\omega_k, k_B T)] \left| \Phi' \left(\omega_L - \frac{\omega_k}{2} \right) \right|^2. \quad (16)$$

In the preresonant case, the polarizability is dominated by the real part, with a functional form corresponding to a dispersive Lorentzian. In this approximation, the derivative Φ' depends on the detuning $\delta = \omega_{res} - (\omega_L - \omega_k/2)$ with respect to full resonance as

$$\Phi' \left(\omega_L - \frac{\omega_k}{2} \right) \propto \frac{1}{\delta^2}, \quad (17)$$

so that a dependence on Huang–Rhys factor and detuning like in Eq. (11) is recovered. In cases involving smooth structureless absorption bands with a full width at half maximum (FWHM) much larger than the frequency ω_k of the vibrational mode, even at resonance the Raman cross section is essentially proportional to

$$\frac{d\sigma(\omega_L)}{d\Omega} \propto S_k (\hbar\omega_k)^2 [1 + n_{th}(\hbar\omega_k, k_B T)] \quad (18)$$

with a further dependence on the mode k introduced only via the weakly frequency-dependent derivative of the polarizability in the form $|\Phi'(\omega_L - \frac{\omega_k}{2})|^2$.

As discussed below, DIP has a highly structured absorption band with several vibronic sublevels of the Frenkel exciton arising from the strong HOMO-LUMO excitation of each molecule.⁸ Therefore, for preresonant excitation at $\lambda = 632.8\text{nm}$ (1.96 eV), Eqs. (11) and (18) remain a valid approximation, whereas for resonant excitation at $\lambda = 532.1\text{nm}$

(2.33 eV), the refined analysis according to Eq. (12) has to be taken into account.

E. Sum frequencies

Treating two different modes $k \neq l$ explicitly, the detuning according to Eq. (7) is generalized to

$$\delta = \omega_{00} + \sum_{j \neq k, j \neq l} m_j^{(e)} \omega_j - \omega_L. \quad (19)$$

Raman scattering involving simultaneous excitation of the modes at ω_k and ω_l via the intermediate state at $\epsilon = m_k^{(e)} \omega_k + m_l^{(e)} \omega_l$ is governed by the product of the respective matrix elements $\langle 1_k^{(g)} | m_k^{(e)} \rangle \langle m_k^{(e)} | 0_k^{(g)} \rangle$ and $\langle 1_l^{(g)} | m_l^{(e)} \rangle \langle m_l^{(e)} | 0_l^{(g)} \rangle$ according to Eq. (6) and a Taylor expansion of $1/[\omega_m - \omega_i - \omega_L - i\gamma]$ analogous to Eq. (8):

$$\frac{1}{\omega_m - \omega_i - \omega_L - i\gamma} = \frac{1}{\delta + \epsilon - i\gamma} \approx \frac{1}{\delta} \left[1 - \frac{\epsilon}{\delta} + \left(\frac{\epsilon}{\delta} \right)^2 \right]. \quad (20)$$

The second order term contains a contribution

$$\frac{1}{\delta} \left[1 - \dots + \frac{2m_k^{(e)} m_l^{(e)} \omega_k \omega_l}{\delta^2} + \dots \right] \quad (21)$$

Based on similar algebra as in Eq. (9) for the first order Raman scattering, one finds

$$\frac{2\sqrt{S_k S_l} \omega_k \omega_l}{\delta^3} \quad (22)$$

for the respective term, and the Raman cross section generalizing Eq. (10) becomes

$$\frac{d\sigma(\omega_L)}{d\Omega} = \frac{\omega_L \omega_s^3}{16\pi^2 \epsilon_0^2 \hbar^2 c^4} (\mathbf{e}_s \cdot \hat{\boldsymbol{\mu}}_{ge})^2 \times (\mathbf{e}_L \cdot \hat{\boldsymbol{\mu}}_{eg})^2 S_k S_l \omega_k^2 \omega_l^2 \left(\frac{2}{\delta^3} \right)^2 \quad (23)$$

At finite temperature, the cross sections for Stokes scattering from sum frequencies $\omega_k + \omega_l$ have to be corrected by $[1 + n_{th}(\hbar\omega_k, k_B T)][1 + n_{th}(\hbar\omega_l, k_B T)]$, and frequency differences like $\omega_k - \omega_l$ by $[1 + n_{th}(\hbar\omega_k, k_B T)]n_{th}(\hbar\omega_l, k_B T)$. Due to the steeper dependence on the detuning according to $\langle 1/\delta^3 \rangle^2$, second order Raman scattering under preresonant conditions is expected to be much weaker than first order scattering. Under full resonance, the assumptions underlying the series expansion in Eq. (21) are no more valid, and a closed analytical expression cannot be obtained. To leading order, Raman cross sections at the sum or difference frequency of two modes ω_k and ω_l remain proportional to the product of the respective Huang–Rhys factors, or $S_k S_l$.

III. EXPERIMENTAL

A. Film preparation

A clean Au(111) surface was prepared by a very gentle and brief Ar⁺ ion bombardment (500 V), followed by annealing in UHV at approximately $T = 900$ K. On this sub-

strate held at room temperature, thin films of diindenoperylene (DIP) were prepared by organic molecular beam deposition (OMBD) in UHV using strictly controlled evaporation conditions (evaporation rate 3 Å/min). During growth the deposition rate was monitored using a quartz microbalance, and after DIP deposition the nominal thickness of about 4 nm was cross-checked by using the attenuation of the x-ray photoemission signal from the gold substrate.

For the DIP films grown on SiO₂, a 1 mm thick oxidized Si(100) wafer served as a substrate.⁸ The DIP films were grown by OMBD under UHV conditions at a base pressure of 2×10^{-10} mbar with the substrate held at a temperature of $T = 400$ K. The growth rate of about 2 Å/min was monitored via a water-cooled quartz-crystal microbalance. For these growth conditions the crystalline structure is well ordered along the surface normal, corresponding to the β phase.^{4,5}

B. Film structure

As discussed elsewhere in more detail, for DIP films grown on SiO₂ substrates held above room temperature, the molecules adsorb with the long axis tilted by about $\theta = 17^\circ$ against the substrate normal.⁸ The crystallites have a random azimuthal orientation, so that after averaging over the crystallites in the illuminated area, the largest component of the dielectric tensor coincides with the substrate normal, whereas the two in-plane components are equal and much smaller in size.

Scanning tunneling microscopy of DIP monolayers on gold has determined that DIP adsorbs with the molecular plane parallel to the substrate surface.²³ In thicker DIP films, each type of substrate defines a specific structure with a fraction of lying-down molecules (λ phase) and standing molecules (σ phase), with a predominance of the λ phase on polycrystalline gold and of the σ phase on nonmetallic substrates.^{7,24} More specifically, complementary investigations of DIP films on polycrystalline gold performed with x-ray scattering and transmission electron microscopy indicate that in at least 74% of the film volume, the long axis of DIP remains parallel to the substrate.²⁴ On the other hand, for film thicknesses above 1 nm, x-ray absorption spectroscopy yields an average tilting angle between the molecular normal and the substrate normal in the range between 40 and 50°.²⁵ Recent highly resolved photoemission electron microscopy investigations on thin films of DIP deposited on Au(111) single crystals²⁶ have revealed that, although the first monolayer of DIP is adsorbed with the molecular plane parallel to the substrate, the structure of subsequent layers is a compromise between intermolecular interactions and substrate–molecule interactions. As a consequence, the molecules arrange themselves in a herringbone fashion as in the bulk β phase,⁵ but with the longest lattice vector \mathbf{c} of the crystal unit cell parallel to the substrate plane.²⁶

In the context of Raman spectroscopy close to resonant with the HOMO–LUMO transition, this film structure defines a preferential orientation of the HOMO–LUMO transition dipoles along the long molecular axes parallel to the

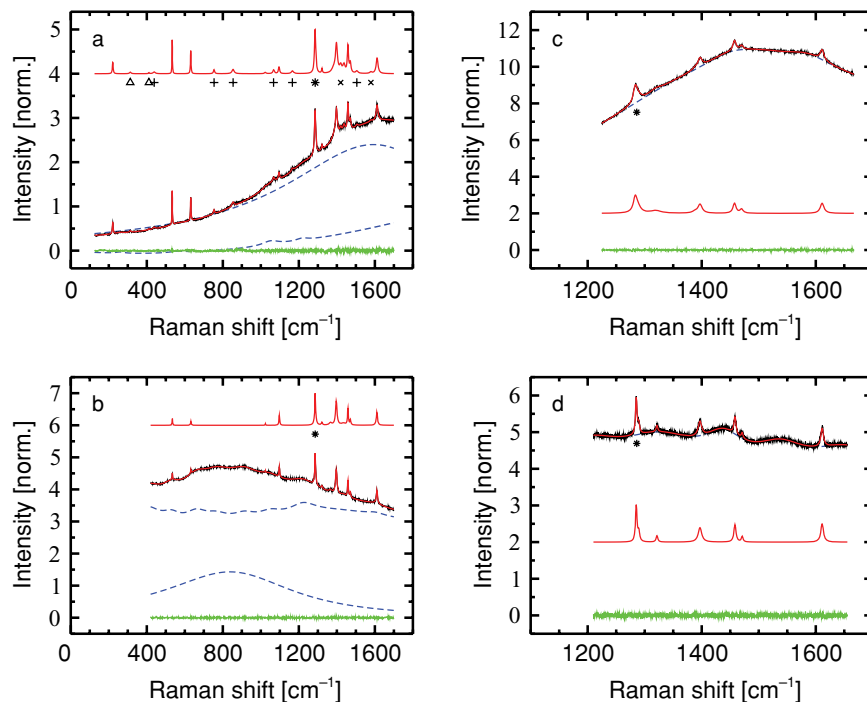


FIG. 1. Raman spectra of two types of DIP films. (a) Resonant Raman spectra of a 4 nm thick DIP film grown on Au, obtained resonantly with a Nd:YAG laser at $\lambda = 532.1$ nm (2.33 eV), (b) preresonant Raman spectra of the same DIP film on Au obtained with a He-Ne laser at $\lambda = 632.8$ nm (1.96 eV), (c) resonant Raman spectra of a 30 nm thick DIP film grown on SiO_2 , obtained at $\lambda = 532.1$ nm (2.33 eV), (d) preresonant Raman spectra of the same DIP film on SiO_2 obtained at $\lambda = 632.8$ nm (1.96 eV). The different curves represent observed spectra (black) and superimposed fit (red), contributions to PL background (blue dashed), fit residuum (green), and fitted Raman spectra without PL background (red, shifted for clarity). In each panel, all curves are normalized to the largest intensity of the fitted Raman spectra at 1286 cm^{-1} , marked with *. In panel a, combinations of breathing modes are marked with + for sums and Δ for differences, and candidates for second harmonics of modes of lower symmetry with \times . These mode combinations do not give significant Raman cross sections in panels b, c, and d.

substrate surface. This indicates that the shape of the dielectric function for light polarization parallel to the substrate surface corresponds to the largest element of the dielectric tensor observed for DIP films grown on oxidized silicon, where this largest optical response occurred for electric field along the substrate normal.⁸ Due to the random azimuthal orientation of the DIP crystallites on gold, the in-plane dielectric function has to be reduced by a prefactor of about 1/2 with respect to the out-of-plane component of the dielectric tensor of DIP films grown on SiO_2 .

C. Optical instrumentation and data analysis

Raman spectra of freshly prepared samples were measured *ex situ* in back-scattering geometry using a confocal Raman spectrometer (LabRam HR 800, Horiba Jobin Yvon) equipped with a frequency-doubled Nd:YAG laser (532.1 nm), a He-Ne laser (632.8 nm), and a CCD detector. The laser beam was focused onto the samples by a 100-fold magnifying microscope objective (NA=0.9) leading to a spot size of about $1 \mu\text{m}$ in diameter. The spectral resolution was about 2 cm^{-1} . In order to prevent radiation damage, a reduced laser power ($< 1 \text{ mW}$) was used. The polarization-dependent Raman spectra collected in crossed (I_{ij}) and parallel (I_{ii}) polarization configuration with respect to the incident laser light did not reveal substantial differences, so that the following discussion will be restricted to spectra obtained for parallel polarization. The analysis of the spectra was performed using the Levenberg–Marquardt algorithm for fitting the Raman

profiles together with a frequency-dependent background, as implemented in the GNU PLOT software package.

D. Resonant Raman spectra for DIP on Au

Figure 1(a) shows resonant Raman spectra recorded *ex situ* with a laser at 532.1 nm (2.33 eV) from a freshly prepared DIP film on Au(111). The spectra reveal a strong PL background dominated by a broad Lorentzian band centered at 1620 cm^{-1} below the laser line, or 2.13 eV on an absolute energy scale, and a rising tail of PL bands at lower energies. Both parts of the background resemble PL features of DIP observed earlier.²⁷ For simplicity, fluctuations of the smooth background of unknown origin were fitted to a few very broad Lorentzians. The various sharp Raman modes were fitted to Lorentzians with FWHM between 2.5 and 27 cm^{-1} .

The Raman spectra before and after subtracting the PL background are shown in Fig. 1(a), and the positions and intensities of the most prominent Raman bands are summarized in Table I. The spectra visualized in Fig. 1(a) are normalized to the height of the largest scattering cross section at 1285 cm^{-1} . For this specific mode, the splitting into a dominating cross section at 1285 cm^{-1} and a much smaller contribution at 1289 cm^{-1} was analyzed in detail, and the sum of these two cross sections was used for the normalization of the measured intensities in Table I.

Out of the 24 A_g breathing modes of a rectangular DIP molecule, 20 occur in the region covered by the measured Raman spectra. The most intense among the observed Raman

TABLE I. Positions of the Raman modes observed 4 nm thick DIP films grown on Au for excitation at $\lambda = 532.1$ nm (2.33 eV) and $\lambda = 632.8$ nm (1.96 eV), together with the calculated breathing modes and their Huang–Rhys factors S obtained with a constrained DFT scheme ($n_{\text{HOMO}} = n_{\text{LUMO}} = 1$) at the B3LYP/TZVP level discussed in Sec. IV C, with mode frequencies scaled by a factor of 0.973 and Huang–Rhys factors scaled by $1/0.973$, keeping the reorganization energy of each mode constant. All intensities are normalized to the sum over the mode pair at 1285 and 1291 cm^{-1} . Further details of the DFT calculations are discussed in Sec. IV. Several Raman peaks are assigned to sums or differences of breathing modes (third column).

$\lambda = 532.1$ nm			$\lambda = 632.8$ nm		Constrained DFT		
Mode cm^{-1}	Int. 1	Combination cm^{-1}	Mode cm^{-1}	Int. 1	Mode cm^{-1}	S 1	$S(\hbar\omega)^2$ 1
221	0.160				215	0.339	0.026
313	0.040	534 – 221					
411	0.015	631 – 221					
439	0.065	221 + 221					
					449	0.003	0.001
534	0.243		534	0.104	529	0.127	0.059
631	0.234		632	0.088	626	0.052	0.034
					697	0.002	0.002
754	0.084	534 + 221					
					833	0.001	0.001
854	0.163	631 + 221					
					995	0.000	0.000
1023	0.035		1024	0.022	1021	0.002	0.003
1067	0.105	534 + 534					
1096	0.140		1097	0.251	1089	0.018	0.035
					1155	0.000	0.000
1166	0.105	534 + 631					
					1208	0.001	0.002
1285	0.955		1286	1.000	1277	0.371	1.000
1291	0.045						
1322	0.067		1321	0.093	1312	0.054	0.154
					1314	0.001	0.003
			1366	0.184			
1383	0.292						
1398	0.980		1397	1.138	1387	0.137	0.436
1420	0.271				2×703	–	–
1437	0.310		1435	0.263	1421	0.080	0.267
1458	0.544		1458	0.438	1447	0.142	0.491
1471	0.246		1471	0.144			
1505	0.092	1285 + 221					
1579	0.057				2×789	–	–
					1567	0.005	0.020
					1584	0.024	0.100
1612	0.515		1610	0.509	1592	0.094	0.394

cross sections can be assigned to the calculated A_g modes of a DIP molecule tabulated in Table I; compare Sec. IV for computational details. Besides the breathing modes, several sum frequencies can be observed, involving mainly the lowest A_g mode at 221 cm^{-1} .

E. Preresonant Raman spectra for DIP on Au

With a laser line at 632.8 nm (1.96 eV) significantly below the lowest subband of the dielectric function at 2.25 eV, DIP films can hardly be excited,^{8,28} so that the PL background is suppressed by several orders of magnitude. Due to the steep

dependence of the Raman cross sections on the detuning according to Eqs. (10) and (11), the intensity of the Raman signal is reduced as well. Figure 1(b) presents the preresonant Raman spectra obtained at this wavelength. The sharp Raman lines are superimposed to a fluctuating background dominated by a broad band about 0.1 eV below the laser line. In this energy region, several broad PL bands from DIP have been observed, but the background in Fig. 1(b) does not coincide with the respective energies, so that no assignment to specific PL features can be made. Instead, the broad band at about 800 cm^{-1} below the laser line corresponding to an energy of about 1.86 eV might reveal PL from the gold substrate.²⁹ Below 400 cm^{-1} , the background becomes even more structured, so that the cross section of the lowest breathing mode at 221 cm^{-1} could not be analyzed in detail. As no other prominent features are expected in this region, it has been excluded from Fig. 1(b) and Table I.

A comparison of the resonant and the preresonant Raman spectra in Figs. 1(a) and 1(b) reveals that the same breathing modes dominate the spectra. Nevertheless, there are also pronounced differences: First, a rather strong Raman feature at 1420 cm^{-1} could only be observed under resonant excitation at 532.1 nm, second, the splitting of two breathing modes into the pairs at 1285 and 1291 cm^{-1} and at 1383 and 1397 cm^{-1} could not be resolved off-resonantly, and third, all Raman peaks assigned to sum frequencies or difference frequencies do not contribute significantly under off-resonant excitation.

F. Raman spectra for DIP on SiO₂

In the following, the discussion of Raman spectra obtained from 30 nm thick DIP film grown on SiO₂ will be restricted to the region 1200–1650 cm^{-1} contributing to the progression over an effective internal vibration at about 170 meV (1371 cm^{-1}) observed in solution spectra.⁸ Resonant Raman spectra obtained from these thicker DIP films are shown in Fig. 1(c). With respect to the spectra in Fig. 1(a) obtained at the same laser energy of 2.33 eV, the PL background is about 3.5 times more prominent, indicating a larger PL yield arising from a better crystallinity of the thicker DIP films and a smaller influence of PL quenching at the substrate/DIP interface. The strongest Raman features tabulated in Table II coincide with the vibrational modes contributing to the DIP films on gold, and they can again be assigned to A_g breathing of the free molecule.

Preresonant Raman spectra obtained at a laser energy of 1.96 eV are shown in Fig. 1(d). The oscillatory features of the background are modeled by a sum of broad Lorentzians, so that a fit of the narrow cross sections arising from the breathing modes can be presented separately.

As shown in Table II, both the resonant Raman spectra in Fig. 1(c) and the preresonant Raman spectra in Fig. 1(d) can be assigned to the A_g breathing modes with the largest calculated Huang–Rhys factors. Deviations from the Raman cross sections expected according to Eqs. (11) and (17) remain much smaller than for the DIP film grown on a gold substrate. Therefore, we conclude that Raman spectra from DIP

TABLE II. Positions of the Raman peaks observed on 30 nm thick DIP films grown on SiO₂ for excitation at $\lambda = 532.1$ nm (2.33 eV) and $\lambda = 632.8$ nm (1.96 eV), together with the calculated breathing modes and their Huang–Rhys factors S obtained with a constrained DFT scheme ($n_{\text{HOMO}} = n_{\text{LUMO}} = 1$) at the B3LYP/TZVP level discussed in Sec. IV C. The calculated mode frequencies scaled by a factor of 0.973 and Huang–Rhys factors scaled by $1/0.973$, keeping the reorganization energy of each mode constant.

$\lambda = 532.1$ nm		$\lambda = 632.8$ nm		Constrained DFT		
Mode cm ⁻¹	Int. 1	Mode cm ⁻¹	Int. 1	Mode cm ⁻¹	S 1	$S(\hbar\omega)^2$ 1
				1208	0.001	0.002
1283	0.587	1285	0.760	1277	0.371	1.000
1288	0.413	1290	0.240			
1319	0.315	1321	0.151	1312	0.054	0.154
1388	0.086					
1397	0.430	1397	0.711	1387	0.137	0.436
1457	0.344	1458	0.506	1447	0.142	0.491
1470	0.143	1471	0.125			
				1567	0.005	0.020
				1584	0.024	0.100
1611	0.437	1611	0.677	1592	0.094	0.394

films on weakly reactive substrates like SiO₂ or TiO₂³⁰ follow the behavior expected for a free molecule rather closely.

IV. ELECTRONIC TRANSITIONS AND DEFORMATION OF EXCITED MOLECULE

Earlier investigations confirm that DFT gives accurate results for the ground state properties of polycyclic hydrocarbons, including very large molecules like terylene.³¹ Furthermore, calculations of the lowest electronic excitations with time-dependent DFT (TD-DFT) have revealed a reasonable agreement with the observed transition energies.^{32–34} In TD-DFT calculations based on the B3LYP hybrid functional,^{35,36} systematic deviations arising from the DFT and Hartree–Fock weights in this functional compensate to a large extent, so that the resulting transition energies are particularly reliable. Nevertheless, due to the wrong asymptotics of the exchange–correlation functional, TD-DFT produces systematic deviations in specific cases. As an example, the ordering of ¹L_a and ¹L_b transitions may differ from the observed spectra,³⁷ but in our case where a single dipolar transition of DIP dominates the optical response within the energy range of interest, such shortcomings are hardly relevant.

In all the DFT and TD-DFT calculations presented below, we have used the B3LYP hybrid functional, as implemented in the TURBOMOLE 5.9 program package.^{38–40} Our variational basis has triple- ζ quality with polarized basis functions (TZVP, [5s3p1d|11s6p1d]).⁴¹

A. Electronic transitions

The geometry of DIP has been optimized with B3LYP/TZVP, and the vertical transition energies have been computed with TD-DFT using the same functional and variational basis set. The lowest dipole-active transitions resulting from this method are tabulated in Table III, revealing

TABLE III. Calculated dipole-active transitions of a D_{2h} -symmetric DIP molecule, where B_{1u} excitations have their transition dipole along the long axis, and B_{2u} excitations along the short axis. Transition energies and oscillator strengths have been obtained with TD-DFT using B3LYP/TZVP.

Transition	Energy (eV)	f_{osc} (1)
$1B_{1u}$	2.35	0.764
$1B_{2u}$	2.97	0.001
$2B_{2u}$	3.71	0.036
$2B_{1u}$	3.94	0.051
$3B_{2u}$	4.00	0.022
$3B_{1u}$	4.22	0.587
$4B_{2u}$	4.31	0.059
$4B_{1u}$	4.51	0.640
$5B_{2u}$	4.81	0.070
$5B_{1u}$	4.91	0.321

that there are no strong transitions within about 1.8 eV above the HOMO–LUMO transition at 2.35 eV. Therefore, Raman spectra excited with laser lines below 2.5 eV are dominated by the resonant or preresonant enhancement of the HOMO–LUMO transition, so that the deformation pattern in the relaxed excited geometry associated to this transition will determine the relative cross sections of different breathing modes.

B. Relaxed excited geometry

As the lowest transition obtained with TD-DFT involves mainly HOMO and LUMO, a constrained calculation of the excited geometry using fixed occupations $n_{\text{HOMO}} = n_{\text{LUMO}} = 1$ can be compared with a TD-DFT optimization of the relaxed excited geometry. The deformation patterns resulting from both approaches have a similar shape, but from a previous analysis of the absorption of dissolved DIP chromophores and other perylene compounds, it was found that the deformation obtained with the constrained scheme is quantitatively more reliable: TD-DFT gives a too small deformation of the relaxed excited geometry.^{8,9}

In Fig. 2, we compare the deformation obtained under the constraint $n_{\text{HOMO}} = n_{\text{LUMO}} = 1$ with the frontier orbitals. The elongation of the various bonds in DIP follows a simple rule: in cases where a bonding lobe of the HOMO is replaced by a repulsive node of the LUMO, the bond length increases, and bonds where a repulsive node of the HOMO is replaced by a bonding lobe of the LUMO react with a shortening of the respective interatomic distance. The increased strength of bonds along the long axis of the molecule results in a shortening along this direction, whereas the additional nodes of the LUMO roughly parallel to the long axis result in an increase in the width of the excited molecule along its short axis.⁴²

C. Elongation of breathing modes

The calculated deformation of an excited DIP molecule is projected onto the vibrational eigenvectors of the A_g breathing modes, defining in turn the respective Huang–Rhys factors. A weighted average of the strong Raman modes above 900 cm⁻¹ defines a progression over consecutive subbands of

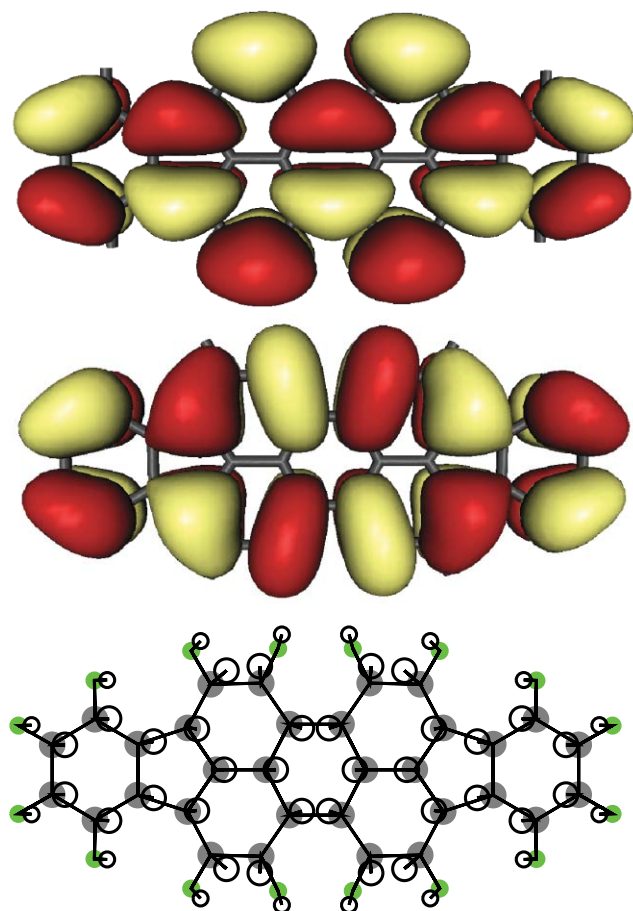


FIG. 2. Deformation pattern of DIP in its relaxed excited geometry (lower), and frontier orbitals involved in this transition: LUMO (upper) and HOMO (middle). In the lower panel, filled circles correspond to the ground state geometry and open circles visualize the deformation pattern in the relaxed excited geometry, multiplied by a scaling factor of 20 (Ref. 42).

an *effective* vibrational mode as observed in the optical response of dissolved molecules.^{8,9,43,44} Based on a constrained DFT scheme with $n_{\text{HOMO}} = n_{\text{LUMO}} = 1$, the sum over the Huang–Rhys factors for modes above 900 cm^{-1} gives an effective Huang–Rhys factor $S_{\text{eff}} = \sum_k S_k = 0.93$ for an effective mode $\hbar\omega_{\text{eff}} = \sum_k S_k \hbar\omega_k / S_{\text{eff}} = 1371 \text{ cm}^{-1} = 170 \text{ meV}$, in good agreement with the observed vibronic bands of dissolved DIP with $S_{\text{eff}} = 0.87$.⁸ A TD-DFT calculation of the relaxed excited geometry significantly underestimates the deformation, resulting in an effective Huang–Rhys factor of only $S_{\text{eff}} = 0.64$, well below the value observed for dissolved DIP.^{8,9}

Out of the 20 calculated breathing modes within the frequency range covered by the experimental Raman spectra, 11 can be assigned to observed features, including nine modes with substantial Huang–Rhys factors above 0.05. Using a common scaling factor of 0.973 for all calculated mode frequencies recommended for the B3LYP functional,⁴⁵ the average deviation between calculated and measured modes is -9 cm^{-1} , or -0.8% . For the specific case of DIP, this residual deviation reveals that a scaling factor of 0.981 accounting for the influence of anharmonicities would be the best choice, so that the average deviation would vanish, and the average absolute deviation would be reduced to 4 cm^{-1} .

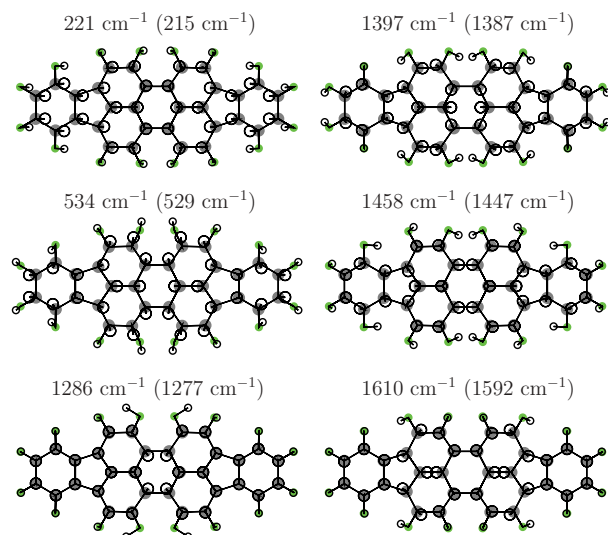


FIG. 3. Elongation patterns of the six breathing modes with the largest calculated Huang–Rhys factors, with observed and calculated positions. The calculated values are given in parentheses, corresponding to B3LYP/TZVP frequencies scaled by a factor of 0.973.

The elongation patterns of several breathing modes resemble perylene and 3,4,9,10-perylene-tetracarboxylic dianhydride (PTCDA).^{43,46} The six breathing modes with the largest calculated Huang–Rhys factors are visualized in Fig. 3, with signs derived from the projection of the vibrational eigenvectors onto the deformation pattern in Fig. 2. The lowest mode observed at 221 cm^{-1} (calculated at 215 cm^{-1}) corresponds to a shortening of the molecule, reproducing most of the atomic elongations of the indeno groups along the long axis. The mode at $534 (529) \text{ cm}^{-1}$ increases the width of the perylene core together with a shrinking of the central hexagon along the long axis. In its elongation in the relaxed excited geometry, these aspects dominate over the motion of the hexagonal part of the indeno groups opposed to the deformation visualized in Fig. 2. The four modes in the range $1286 (1277) \text{ cm}^{-1}$ to $1610 (1592) \text{ cm}^{-1}$ are combinations of C–C stretching motion with C–H bending. The lowest of the four seems to be dominated by C–H bending, but it is elongated via the shrinking of the central hexagon of the molecule. Toward modes with higher frequencies, the contribution of the hydrogen atoms are reduced, so that the elongation patterns resemble optical phonons in graphite. The highest mode at $1610 (1592) \text{ cm}^{-1}$ contains several adjacent atoms moving in opposite directions, as for the optical phonon of graphite at the Γ point of the Brillouin zone. With respect to a similar mode pattern for perylene and PTCDA, the contributions on the pentagonal groups shift the frequency to a somewhat larger value.^{43,46}

D. Comparison between measured and calculated cross sections

The Stokes Raman cross sections of DIP on Au will first be analyzed in terms of Eqs. (11) and (18) (compare the last column in Table I). Among the strongest Raman cross sections observed in the preresonant case (calculated) at 1286 (1277), 1397 (1387), 1435 (1421), 1458 (1447), and 1610

(1592) cm^{-1} , four follow the trends of the calculated Huang–Rhys factors, whereas the mode at 1397 (1387) cm^{-1} is nearly three times stronger than expected. This rather large deviation might be related to a resonance condition between this breathing mode and the second harmonics of a breathing mode at 697 cm^{-1} . Moreover, substantial cross sections at 221 (215), 534 (529), and 631 (626) cm^{-1} correspond to rather large calculated Huang–Rhys factors. The absence of significant Raman cross sections in the vicinity of several further calculated breathing modes is easily understood from their very small Huang–Rhys factors. The mode pair observed at 1458 and 1471 cm^{-1} seems to arise from a Davydov splitting of the calculated breathing mode at 1447 cm^{-1} due to the two basis molecules in the crystal unit cell.

The good agreement between measured and calculated Raman intensities demonstrates that DFT-based deformation patterns in the relaxed excited geometry give a quantitatively meaningful measure for the expected Raman cross sections. However, a few exceptions are worth mentioning: first, the modes at 1397 (1387) cm^{-1} and at 1097 (1089) cm^{-1} give much larger cross sections than expected, and second, two substantial cross sections at 1420 and 1579 cm^{-1} observed only under resonant conditions at 532.1 nm cannot be assigned to any breathing modes or their combinations. Instead, from a comparison with modes of different representations, the one at 1420 cm^{-1} is a candidate for a second order process involving a dipole-active B_{3u} out-of-plane mode with a calculated position of 703 cm^{-1} , and the one at 1579 cm^{-1} for a second order process based on a B_{2g} out-of-plane mode with a calculated position of 789 cm^{-1} . Clearly, these two Raman cross sections cannot be quantified within the theoretical framework summarized in Sec. II. Furthermore, a calculated breathing mode at 1584 cm^{-1} with still relatively large Huang–Rhys factor is not observed. The Raman peak measured under resonant excitation at 1579 cm^{-1} cannot be assigned to this breathing mode because the off-resonant spectra do not show any narrow structure in this region, revealing that the calculated Huang–Rhys factor must be too large.

The Raman modes of DIP films grown on SiO_2 summarized in Table II coincide with the respective modes of thinner DIP films on gold in Table I. They show a closer correspondence with the Raman cross sections expected according to Eqs. (11) and (18), including especially the mode pair at 1388 and 1397 cm^{-1} . Together with the complete absence of substantial cross sections which cannot be assigned to A_g breathing modes, this indicates that the DIP films grown on SiO_2 preserve the spectroscopic properties of a free molecule more closely. A comparison of the two types of DIP films suggests that some of the peculiarities of specific vibrational modes in the DIP films on polycrystalline gold may arise from a modified behavior of molecules in contact to the metal substrate and from a different film structure.

V. RAMAN EXCITATION PROFILES OF DIP ON GOLD

A. Breathing modes

In the following, the polarization function Φ has to be replaced by the in-plane component of the dielectric tensor.

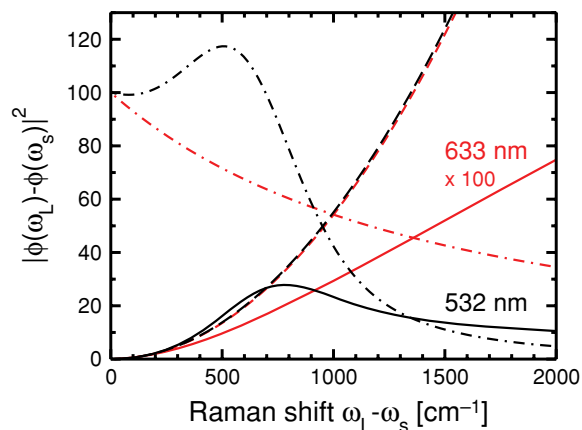


FIG. 4. Squared difference of polarizabilities $|\Phi(\omega_L) - \Phi(\omega_s)|^2$ with Φ according to the larger component of the dielectric tensor of DIP films grown on SiO_2 according to Ref. 8 (solid lines), parabolic approximation (dashed), and ratio between $|\Phi(\omega_L) - \Phi(\omega_s)|^2$ and the parabolic approximation, normalized to 100% at low frequency (dashed-dotted). The non-normalized curves for pre-resonant excitation at 632.8 nm (red) are scaled up by a factor of 100 with respect to resonant excitation at 532.1 nm (black).

From the structure of the DIP films on gold summarized in Sec. III B, this in-plane component can be related to the large out-of-plane component of the dielectric tensor observed for DIP films grown on SiO_2 substrates,⁸ so that the polarizability function Φ will be chosen accordingly.

Ignoring all the other ingredients of Eq. (12), the following discussion of the Raman excitation profiles will concentrate on the absolute square of the difference of polarizabilities,

$$|\Phi(\omega_L) - \Phi(\omega_s)|^2. \quad (24)$$

Based on the known shape of Φ ,⁸ Eq. (24) can easily be evaluated for each Raman shift $\omega_L - \omega_s$. As shown in Fig. 4, for small values of $\omega_L - \omega_s$ the difference $|\Phi(\omega_L) - \Phi(\omega_s)|$ is linear in $\omega_L - \omega_s$, so that its square $|\Phi(\omega_L) - \Phi(\omega_s)|^2$ starts proportional to a parabola $(\omega_L - \omega_s)^2$ as in the simplified Raman cross section according to Eq. (11). For pre-resonant excitation, the function $|\Phi(\omega_L) - \Phi(\omega_s)|^2$ drops monotonously with respect to the parabolic reference, reaching a value of about 41% for the highest breathing mode observed at 1610 cm^{-1} . Under resonant excitation at 532.1 nm, the polarizability $\Phi(\omega_L)$ at the laser frequency falls into the valley between the Gaussian subbands of the dielectric function at $E_{00} = 2.25$ eV and at $E_{01} = 2.42$ eV, whereas the polarizability $\Phi(\omega_s)$ is sampled across the E_{00} resonance. Therefore, for small arguments $\omega_L - \omega_s$, the difference $|\Phi(\omega_L) - \Phi(\omega_s)|$ starts steeper than linear and $|\Phi(\omega_L) - \Phi(\omega_s)|^2$ steeper than the parabolic approximation, but as soon as $\hbar\omega_s$ drops below E_{00} at a Raman shift of about 600 cm^{-1} , the ratio $|\Phi(\omega_L) - \Phi(\omega_s)|^2/(\omega_L - \omega_s)^2$ falls to values far below one, down to only 9% for the highest observed Raman mode at 1610 cm^{-1} .

The deviations of the observed Raman cross sections from $S(\hbar\omega)^2$ as tabulated in Table I can be interpreted with the Raman excitation profiles in Fig. 4. Under pre-resonant excitation at 632.8 nm, the high frequency region between 1285 and 1610 cm^{-1} is only weakly affected

because the ratio $|\Phi(\omega_L) - \Phi(\omega_s)|^2/(\omega_L - \omega_s)^2$ drops only from 47% down to 41%. Nevertheless, as this ratio rises to 66% at 632 cm^{-1} and 70% at 534 cm^{-1} , these low frequency modes will be enhanced with respect to the reference mode at 1285 cm^{-1} , as observed. Under resonant excitation at 532.1 nm, at 1285 cm^{-1} the ratio $|\Phi(\omega_L) - \Phi(\omega_s)|^2/(\omega_L - \omega_s)^2$ has dropped to only 18%, so that the modes at 632 cm^{-1} and below seem to be particularly enhanced. More precisely, for Raman modes at low frequencies, the parabolic approximation to $|\Phi(\omega_L) - \Phi(\omega_s)|^2$ still remains reasonable, whereas for the reference mode at 1285 cm^{-1} the value of this function is much smaller, so that the respective cross section is strongly reduced, as observed. Residual deviations between observed and calculated Raman cross sections may be associated to modified optical properties in the first few monolayers, as observed recently for the growth of different molecular semiconductors even on nonreactive substrates.⁴⁷

B. Sums and differences of breathing modes

Even under resonant excitation at 532.1 nm, the Raman cross sections at sums $\omega_k + \omega_l$ and differences $\omega_k - \omega_l$ of two breathing modes at ω_k and ω_l remain much smaller than the first order scattering of each mode contributing. For pairs of Raman peaks involving the same breathing modes, like the ones at 754 cm^{-1} and 313 cm^{-1} interpreted as $\omega_k \pm \omega_l = 534 \pm 221 \text{ cm}^{-1}$, the intensities should scale as $[1 + n_{th}(\hbar\omega_k, k_B T)][1 + n_{th}(\hbar\omega_l, k_B T)]$ and $[1 + n_{th}(\hbar\omega_k, k_B T)]n_{th}(\hbar\omega_l, k_B T)$. Based on the thermal occupation $n_{th}(\hbar\omega_l, k_B T) = 0.53$ for the lowest breathing mode at 221 cm^{-1} , the ratio between the cross sections at the sum and difference frequencies should be about 2.9, in reasonable agreement with the observed ratio of 2.1. Also for the two Raman peaks at 854 and 411 cm^{-1} , an interpretation as $631 \pm 221 \text{ cm}^{-1}$ should give the same intensity ratio of 2.9, but the agreement with the observed ratio of 5.6 seems somewhat less convincing. Presumably, such deviations can be related to more complicated but unknown resonance profiles for sums and differences of strongly elongated breathing modes.

VI. CONCLUSION

In the present work, experimental Raman spectra obtained on thin DIP films deposited on gold or SiO_2 were interpreted with DFT-based calculations of the deformation of a single DIP molecule in its relaxed excited geometry. From a comparison with the vibronic subbands of the absorption spectra determined on dissolved DIP molecules, the results from the constrained DFT calculation turned out to be more reliable, so that they have been used throughout the present analysis of resonant and preresonant Raman spectra. Due to the strongly modulated dielectric function of DIP thin films, for a quantitative comparison of the observed Raman signals of breathing modes at low and high frequencies, it was necessary to calculate the Raman resonance profiles directly from the frequency-dependent dielectric response. This analysis has provided some quantitative insight into the apparent resonant enhancement of the cross sections arising for breathing modes at rather low frequencies with respect to the strongly

elongated high frequency modes in the region between 1286 and 1610 cm^{-1} . As expected, simpler approximations for the calculated Raman cross sections have remained more reliable for preresonant excitation. A few of the observed structures in resonantly enhanced Raman spectra have been assigned to sums or differences of strongly elongated breathing modes. Under preresonant excitation, the respective mode combinations have remained below the detection limit because their intensities drop with a higher inverse power of the detuning. In relatively thick DIP films grown on SiO_2 , the expected spectroscopic signature of an excited molecule was followed more closely with respect to the much thinner DIP films deposited on gold. On the other hand, the specific structure of DIP on gold favored Raman signals from combinations of breathing modes, a feature which could not be observed in the thicker DIP film on silicon oxide with its larger and differently oriented crystallites. Therefore, the different structures of both types of samples have allowed us to reveal several complementary aspects of the respective Raman spectra.

ACKNOWLEDGMENTS

We thank Jens Pflaum for purification of the diindenoperylene used in the present work. Financial support from EPSRC and the DFG Priority Programme 1121 OFETs through the projects Scho 521/5 and Schr 700/13-1 is gratefully acknowledged.

- ¹J. von Braun and G. Manz, *Ber. d. D. Chem. Gesellschaft* **70**, 1603 (1937).
- ²N. Karl, "Charge carrier mobility in organic crystals," in *Organic Electronic Materials*, edited by R. Farchioni and G. Grosso (Springer, Berlin, 2001).
- ³A. K. Tripathi and J. Pflaum, *Appl. Phys. Lett.* **89**, 082103 (2006).
- ⁴A. C. Dürr, F. Schreiber, M. Münch, N. Karl, B. Krause, V. Kruppa, and H. Dosch, *Appl. Phys. Lett.* **81**, 2276 (2002).
- ⁵M. A. Heinrich, J. Pflaum, A. K. Tripathi, W. Frey, M. L. Steigerwald, and T. Siegrist, *J. Phys. Chem. C* **111**, 18878 (2007).
- ⁶A. C. Dürr, F. Schreiber, K. A. Ritley, V. Kruppa, J. Krug, H. Dosch, and B. Struth, *Phys. Rev. Lett.* **90**, 016104 (2003).
- ⁷S. Kowarik, A. Gerlach, S. Sellner, F. Schreiber, L. Cavalcanti, and O. Kononov, *Phys. Rev. Lett.* **96**, 125504 (2006).
- ⁸U. Heinemeyer, R. Scholz, L. Gisslén, M. I. Alonso, J. O. Ossó, M. Garriga, A. Hinderhofer, M. Kytka, S. Kowarik, A. Gerlach, and F. Schreiber, *Phys. Rev. B* **78**, 085210 (2008).
- ⁹L. Gisslén and R. Scholz, *Phys. Rev. B* **80**, 115309 (2009).
- ¹⁰M. Pirotta, A. Renn, M. H. V. Werts, and U. P. Wild, *Chem. Phys. Lett.* **250**, 576 (1996).
- ¹¹M. Wewer and F. Stienkemeier, *Phys. Rev. B* **67**, 125201 (2003).
- ¹²M. Wewer and F. Stienkemeier, *J. Chem. Phys.* **120**, 1239 (2004).
- ¹³R. Loudon, *The Quantum Theory of Light*, 3rd ed. (Oxford University Press, Oxford, 2000), Chap. 8.
- ¹⁴A. C. Albrecht, *J. Phys. Chem.* **34**, 1476 (1961).
- ¹⁵B. B. Johnson and W. L. Peticolas, *Ann. Rev. Phys. Chem.* **27**, 465 (1976).
- ¹⁶A. B. Myers, R. A. Mathies, D. J. Tannor, and E. J. Heller, *J. Chem. Phys.* **77**, 3857 (1982).
- ¹⁷J. B. Page and D. L. Tonks, *J. Chem. Phys.* **75**, 5694 (1981).
- ¹⁸J. R. Cable and A. C. Albrecht, *J. Chem. Phys.* **84**, 1969 (1986).
- ¹⁹E. J. Heller, R. L. Sundberg, and D. Tannor, *J. Phys. Chem.* **86**, 1822 (1982).
- ²⁰O. Brafman, C. K. Chan, B. Khodadoost, J. B. Page, and C. T. Walker, *J. Chem. Phys.* **80**, 5406 (1984); C. K. Chan, J. B. Page, D. L. Tonks, O. Brafman, B. Khodadoost, and C. T. Walker, *J. Chem. Phys.* **82**, 4813 (1985).
- ²¹F. Markel, N. S. Ferris, I. R. Gould, and A. B. Myers, *J. Am. Chem. Soc.* **114**, 6208 (1992).
- ²²X. Zhao, J. A. Burt, and J. L. McHale, *J. Chem. Phys.* **121**, 11195 (2004).

- ²³D. G. de Oteyza, E. Barrena, M. Ruiz-Osés, I. Silanes, B. P. Doyle, J. E. Ortega, A. Arnau, H. Dosch, and Y. Wakayama, *J. Phys. Chem. C* **112**, 7168 (2008).
- ²⁴A. C. Dürr, N. Koch, M. Kelsch, A. Rühm, J. Ghijsen, R. L. Johnson, J.-J. Pireaux, J. Schwartz, F. Schreiber, H. Dosch, and A. Kahn, *Phys. Rev. B* **68**, 115428 (2003).
- ²⁵M. B. Casu, I. Biswas, B.-E. Schuster, M. Nagel, P. Nagel, S. Schuppler, and T. Chassé, *Appl. Phys. Lett.* **93**, 024103 (2008).
- ²⁶M. B. Casu, B.-E. Schuster, I. Biswas, C. Raisch, H. Marchetto, T. Schmidt, and T. Chassé, *Adv. Mater.* **22**, 3740 (2010).
- ²⁷M. Heilig, M. Domhan, and H. Port, *J. Lumin.* **110**, 290 (2004).
- ²⁸D. Zhang, U. Heinemeyer, C. Stanciu, M. Sackrow, K. Braun, L. E. Hennemann, X. Wang, R. Scholz, F. Schreiber, and A. J. Meixner, *Phys. Rev. Lett.* **104**, 056601 (2010).
- ²⁹H. Armstrong, D. P. Halliday, and D. P. Hampshire, *J. Lumin.* **129**, 1610 (2009).
- ³⁰V. Presser, B.-E. Schuster, M. B. Casu, U. Heinemeyer, F. Schreiber, K. G. Nickel, and T. Chassé, *J. Raman Spectrosc.* **40**, 2015 (2009).
- ³¹M. Andrzejak, G. Mazur, and P. Petelenz, *J. Mol. Struct.*, **527**, 91 (2000).
- ³²F. Furche and J. Ahlrichs, *J. Chem. Phys.* **117**, 7433 (2002).
- ³³A. J. Sobolewski and W. Domcke, *Phys. Chem. Chem. Phys.* **1**, 3065 (1999).
- ³⁴R. Burcl, R. D. Amos, and N. C. Handy, *Chem. Phys. Lett.* **355**, 8 (1999).
- ³⁵A. D. Becke, *Phys. Rev. A* **38**, 3098 (1988).
- ³⁶C. Lee, W. Yang, and R. G. Parr, *Phys. Rev. A* **37**, 785 (1988).
- ³⁷M. Parac and S. Grimme, *Chem. Phys.* **292**, 11 (2003); S. Grimme and M. Parac, *ChemPhysChem* **4**, 292 (2003).
- ³⁸O. Treutler and R. Ahlrichs, *J. Chem. Phys.* **102**, 346 (1995).
- ³⁹F. Furche and D. Rappoport, "Density functional theory for excited states: Equilibrium structure and electronic spectra," in *Computational and Theoretical Chemistry*, edited by M. Olivucci (Elsevier, Amsterdam, 2005), Vol. 16, Chap. III.
- ⁴⁰R. Ahlrichs, M. Bär, M. Häser, H. Horn, and C. Kölmel, *Chem. Phys. Lett.* **162**, 165 (1989).
- ⁴¹A. Schäfer, C. Huber, and R. Ahlrichs, *J. Chem. Phys.* **100**, 5829 (1994).
- ⁴²The deformation in the relaxed excited geometry as displayed in Fig. 2 of Ref. 8 was misrepresented for several atoms, including especially the indeno groups. Nevertheless, the projection schemes underlying the tables in the present work and the interpretation of the solution spectra in Ref. 8 are both correct. Moreover, Ref. 8 contained a sign error of the hole transfer t_h required in the Frenkel-CT exciton model. The correction of this error improves the agreement between model calculation and measured spectra and leaves the conclusions of Ref. 8 unaffected (compare Table XII and Sec. VIII.F of Ref. 9 for details).
- ⁴³R. Scholz, A. Yu. Kobitski, T.U. Kampen, M. Schreiber, D. R. T. Zahn, G. Jungnickel, M. Elstner, M. Sternberg, and Th. Frauenheim, *Phys. Rev. B* **61**, 13659 (2000).
- ⁴⁴R. Scholz and M. Schreiber, *Chem. Phys.* **325**, 9 (2006).
- ⁴⁵M. D. Halls, J. Velkovski, and H. B. Schlegel, *Theor. Chem. Acc.* **105**, 413 (2001).
- ⁴⁶K. K. Ong, J. O. Jensen, and H. F. Hameka, *J. Mol. Struct. Theochem.* **459**, 131 (1999).
- ⁴⁷U. Heinemeyer, K. Broch, A. Hinderhofer, M. Kytka, R. Scholz, A. Gerlach, and F. Schreiber, *Phys. Rev. Lett.* **104**, 257401 (2010).